



HAL
open science

Atomic-scale modeling of $1/2$ (110)001 edge dislocations in UO₂: Core properties and mobility

Marion Borde, Michel Freyss, Emeric Bourasseau, Bruno Michel, David Rodney, Jonathan Amodeo

► To cite this version:

Marion Borde, Michel Freyss, Emeric Bourasseau, Bruno Michel, David Rodney, et al.. Atomic-scale modeling of $1/2$ (110)001 edge dislocations in UO₂: Core properties and mobility. Journal of Nuclear Materials, 2023, 574, pp.154157. 10.1016/j.jnucmat.2022.154157 . hal-03874424

HAL Id: hal-03874424

<https://hal.science/hal-03874424v1>

Submitted on 28 Nov 2022

HAL is a multi-disciplinary open access archive for the deposit and dissemination of scientific research documents, whether they are published or not. The documents may come from teaching and research institutions in France or abroad, or from public or private research centers.

L'archive ouverte pluridisciplinaire **HAL**, est destinée au dépôt et à la diffusion de documents scientifiques de niveau recherche, publiés ou non, émanant des établissements d'enseignement et de recherche français ou étrangers, des laboratoires publics ou privés.



Distributed under a Creative Commons Attribution - NonCommercial - NoDerivatives 4.0 International License

Atomic-scale modeling of $\frac{1}{2}\langle 110 \rangle\{001\}$ edge dislocations in UO_2 : core properties and mobility

Marion Borde^{a,b,c}, Michel Freyss^d, Emeric Bourasseau^d, Bruno Michel^c,
David Rodney^b, Jonathan Amodeo^{a,e}

^a*Université Lyon, CNRS, INSA Lyon, UCBL, MATEIS UMR5510, 69621
Villeurbanne, France*

^b*Institut Lumière Matière, Université Lyon 1 - CNRS, 69622 Villeurbanne, France*

^c*CEA, DES, IRESNE, DEC, SESC, LSC, 13108 Saint-Paul-Lez-Durance, France*

^d*CEA, DES, IRESNE, DEC, SESC, LM2C, 13108 Saint-Paul-Lez-Durance, France*

^e*Aix-Marseille Université, Université de Toulon, CNRS, IM2NP, 13397
Marseille, France*

Abstract

The dislocation properties of UO_2 , the main nuclear fuel material, are important ingredients to model the mechanical properties and predict nominal and accidental operations of nuclear plant reactors. However, the plastic behaviour of UO_2 is complex with little known about dislocations and other extended defects. In this study, we use a combination of interatomic potential-based atomistic simulations and *ab initio* calculations to investigate the core structure and mobility of the $\frac{1}{2}\langle 110 \rangle\{001\}$ edge dislocation, which controls the plasticity of UO_2 single crystals. Various dislocation cores are obtained and compared, including the classical asymmetric Ashbee core and a so-far unreported core made of an alternation of both variants of the Ashbee core along the dislocation line. This new core, called here *zigzag*, is ubiquitous in molecular dynamics simulations at high temperature in the nominal-to-accidental transient regime (1600 to 2200 K). Molecular dynamics is also used to determine the velocity of the edge dislocation as a function of temperature and stress. A dislocation mobility law is adjusted from the simulations and provides an up-scaling ingredient central to the multi-scale modeling of UO_2 nuclear fuel mechanical properties.

Keywords: UO_2 , dislocation core, dislocation mobility, molecular

Email address: jonathan.amodeo@cnrs.fr (Jonathan Amodeo)

1. Introduction

Uranium dioxide (UO_2 , fluorite structure, $a_0=5.47\text{\AA}$) is the most important fuel material used in pressurised water reactors. During nominal or accidental operations, the temperature in the fuel pellets varies significantly, in a range between 1200 and 2700 K. The induced thermal gradients can generate significant thermomechanical stresses responsible for the deformation and fracture of the pellets [1, 2]. As a consequence, a better understanding of the material viscoplastic behaviour is crucial to provide a solid foundation for predictive multi-scale models of nuclear fuel under irradiation.

The primary slip system of UO_2 single crystals is $\frac{1}{2}\langle 110 \rangle \{001\}$ for which deformation microstructures are typical of materials with a high-lattice friction *i.e.*, they are composed of dislocations with an anisotropic shape made of extended edge segments as well as zigzag portions [3, 4, 5]. As a consequence, the glide of the $\frac{1}{2}\langle 110 \rangle \{001\}$ edge dislocation is known as the rate-limiting process for the deformation of UO_2 single crystals.

Several studies focused on measuring the Critical Resolved Shear Stress (CRSS) of UO_2 single crystals as a function of temperature [6, 7, 8, 9]. Lefebvre and Byron described a typical thermally-activated non-linear decrease of the CRSS in the $\frac{1}{2}\langle 110 \rangle \{001\}$ system down to an athermal stress plateau of about 20 MPa for temperatures above $T_a=1750$ K. Plastic slip in the $\frac{1}{2}\langle 110 \rangle \{110\}$ system was also identified but at larger stresses than for primary slip systems [7, 8]. Finally, a few evidence of $\frac{1}{2}\langle 110 \rangle \{111\}$ dislocations were also reported [8, 10] but no CRSS are available as $\{111\}$ slip is always activated together with $\{001\}$ and/or $\{110\}$ in UO_2 .

To complement experimental investigations, atomistic simulations using semi-empirical potentials were performed. Up to now, they were used to characterize the lattice friction and Peierls barriers, the 0 K Peierls stress as well as to compute CRSS *vs.* temperature profiles [11, 12, 13, 14]. Concerning the various slip systems, CRSS computations at high strain-rate ($\sim 10^8 \text{ s}^{-1}$) using Molecular Dynamics (MD) qualitatively confirmed the experimental evidence about slip systems *i.e.*, the $\frac{1}{2}\langle 110 \rangle \{001\}$ slip is easier than in both other systems. Recently, Soulié *et al.* confirmed using a variable-charge SMTB-Q potential that the edge dislocation requires a larger stress than the screw component to glide in $\{001\}$ [14]. Also, Lunev *et al.* [15] investigated

the mobility of the $\frac{1}{2}\langle 110 \rangle \{001\}$ edge dislocation using several rigid-ion pair potentials including the Yakub [16], Morelon [17] and Potashnikov parameterizations [18] as well as the Cooper, Rushton and Grimes (CRG) many-body potential [19]. While pair potentials are known to describe elastic constants in oxides with limited accuracy (Cauchy rule violation), the Potashnikov potential reproduces best the ionicity parameter $Q = 1 - \exp(-\Delta x^2/4)$ where Δx is the electronegativity variation between U and O atoms [20]. Q is believed to be a critical factor influencing the dislocation mobility in UO_2 [15]. Indeed, Lunev and collaborators have shown that the Yakub and CRG potentials, which both have $Q \sim 0.55$, predict similar dislocation velocities at 2000 K, while larger velocities (up to a factor 3) are obtained with the Morelon and Potashnikov potentials that have a larger $Q=0.689$, closer to the theoretical value ($Q_{th}=0.654$). However, the authors did not provide detailed information on the core configuration they modeled while the $\frac{1}{2}\langle 110 \rangle \{001\}$ edge dislocation can potentially adopt different cores, either neutral or charged [21, 22, 23, 24]. Thus, while the Potashnikov potential appears as a good alternative to more expensive variable-charge potentials, the question of the influence of the core configuration on the mobility of the $\frac{1}{2}\langle 110 \rangle \{001\}$ edge dislocation is still to be clarified.

In the present work, we investigate the core structure and mobility of the $\frac{1}{2}\langle 110 \rangle \{001\}$ edge dislocation in UO_2 using first-principles calculations and classical interatomic potential-based simulations. Various core structures are obtained including neutral and charged configurations. Special attention is paid to the influence of temperature on the fine structure of the dislocation core. The dislocation mobility is computed in the 1600 to 2200 K temperature range characteristic of a nominal-to-accidental transient regime. Simulation results are discussed in light of recent investigations performed on UO_2 dislocation core and mobility.

2. Simulation methods

Atomistic simulations in UO_2 are performed using the Large-scale Atomic/Molecular Massively Parallel Simulator (LAMMPS) package [25]. Interactions between atoms are modeled using the rigid-ion potential adjusted by Potashnikov *et al.* [18] and the SMTB-Q potential [26, 27]. Both were recently used to model dislocations in UO_2 [15, 28, 14]. To handle Coulombic interactions,

Ewald summation [29] and Wolf truncation [30] methods were tested with the Potashnikov potential, leading to quantitatively similar results but a higher computational efficiency with Wolf truncation (see supplementary materials). Also, the SMTB-Q potential is compatible with only this method [26]. We thus used Wolf’s truncation for all molecular simulations presented in the following. The Wolf radius and damping coefficient are set respectively to 11 Å and 0.3 Å⁻¹ for both Potashnikov and SMTB-Q potentials. Short-range interactions with the rigid-ion potential were also cut-off at 11 Å.

First principles density-functional theory (DFT) calculations are performed using the Projector Augmented Wave (PAW) formalism as implemented in the Vienna Ab initio Simulation Package (VASP) [31, 32] using the Perdew–Burke–Ernzerhof (PBE) exchange-correlation functional [33]. An additional on-site Coulombic repulsion is added by including a Hubbard-like term in the Hamiltonian in the rotationally-invariant form proposed by Lichtenstein in order to account for the strong 5f electron correlations [34]. The on-site U and J parameters are set to $U = 4.50$ eV and $J = 0.54$ eV, consistent with the values used in previous works [35, 36, 37, 38]. We also use the Occupation Matrix Control (OMC) scheme to avoid convergence of the self-consistent calculations to metastable states [39]. Calculations are performed at the Γ point with a 500 eV cut-off energy. Spin-polarization is taken into account in a $1\vec{k}$ collinear antiferromagnetic order as an approximation of the $3\vec{k}$ non-collinear antiferromagnetic order of UO₂ below $T_N=31$ K [40], which is not computationally tractable for large supercells.

Atomic configurations are characterized using Ovito [41] and the Polyhedral Template Matching (PTM) crystallographic algorithm [42] applied to the uranium Face-Centered Cubic (FCC) sublattice.

2.1. Dislocation dipole configuration

The $\frac{1}{2}\langle 110\rangle\{001\}$ edge dislocation core structure is investigated using the dislocation dipole method [43, 44]. First, perfect fluorite crystals of size (L_x, L_y, L_z) and oriented along $x = [110]$, $y = [\bar{1}10]$, $z = [001]$ are built using ATOMSK [45]. As illustrated in Figure 1, two edge dislocations with opposite Burgers vectors (\vec{b} along $x = [110]$, dislocation line \vec{l} along $y = [\bar{1}10]$) are then introduced respectively at $(L_x/4 + \delta x, L_z/4 + \delta z)$ and $(3L_x/4 + \delta x, 3L_z/4 + \delta z)$ using the isotropic elastic theory [46]. Dimensions up to $L_x=244.3$

Å, $L_y=92.3$ Å (24b), $L_z=239.4$ Å (402 336 atoms) and $L_x=21.2$, $L_y=7.7$ Å (2b), $L_z=27.2$ Å (330 atoms) are used respectively for classic and DFT simulations. The excess slice of atoms generated by the introduction of the dislocation dipole is removed in the $x = L_x$ region before the box is adapted accordingly. $\delta x = \delta z = 0.25$ Å keeps the neutrality of the excess slice of atoms and avoids the appearance of spurious defects during the introduction of the dislocation dipole. Thus, the charge neutrality of the whole simulation cell is maintained after excess atoms are removed and periodic boundary conditions (PBCs) are applied in the glide direction. In both classic and DFT simulations, the simulation cell is extended of $b/2$ along the x direction and tilted by $-b/2$ (xz orientation) to accommodate the plastic shear introduced by the edge dislocation dipole [47]. At this stage, the resulting configuration is made of two edge dislocations with charged cores, one positive and the other negative. To obtain neutral cores, an extra column of oxygen atoms in the negatively-charged core is moved to the positively-charged one. Unrelaxed configurations are shown in the supplementary materials. In both cases, the simulation cells are neutral and PBCs are used along the three directions of space.

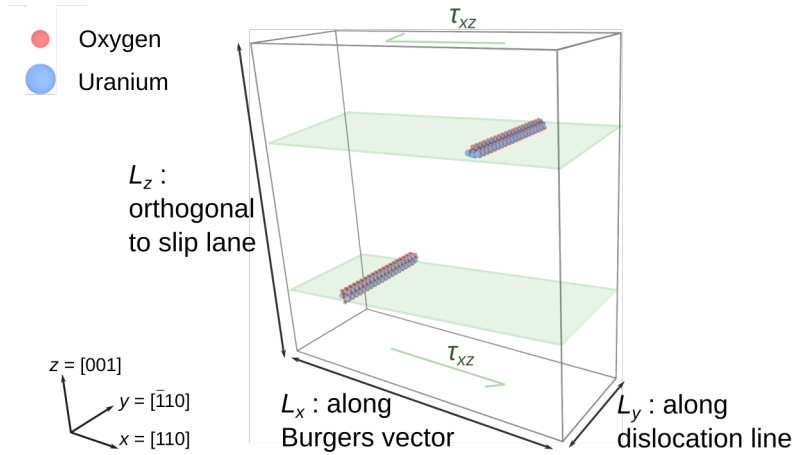


Figure 1: Dislocation dipole simulation cell and crystallographic orientations. The edge dislocation dipole is aligned with the $y=[\bar{1}10]$ direction, the Burgers vectors are along $x=[110]$ and the glide plane has $z=[001]$ normal. 3D periodic boundary conditions are applied. For velocity simulations, a shear stress τ_{xz} is applied to the simulation cell using the Nosé-Hoover barostat.

2.2. Dislocation core relaxation and equilibration

After fabrication of the simulation cell, the internal energy is minimized using the conjugate gradient and FIRE [48] algorithms (the latter being used in molecular statics simulations only). Simulation convergence is obtained using a criterion on the total resulting net force on the system of $f_n = 10^{-10}$, 10^{-6} and 10^{-2} eV/Å respectively for the Potashnikov potential, the SMTB-Q potential and DFT simulations. After energy minimization, the dislocation energy E_{dislo}^X is computed using:

$$E_{dislo}^X = \frac{E^X - N \cdot E_{coh}}{2l}, \quad (1)$$

where E^X is the energy of the cell containing a dislocation dipole after energy minimization, X will be used to denote the type of dislocation core (*e.g.*, Ashbee, Amelincks, ..., see below), N is the number of UO_2 molecules and E_{coh} the cohesive energy. Since in the following, we will only discuss relative dislocation energies between dislocation cores, no elastic correction related to the interactions between the dislocations of the dipole and between these dislocations and their periodic images is needed [49, 44].

To study the thermal stability of the dislocation cores, the relaxed simulation cells are heated up to 2000 K using MD. To that effect, atom velocities are initially randomly set using a gaussian distribution at a temperature of 5 K. After 10 ps equilibration in the NVE ensemble, the system is progressively heated up ($\dot{T} = 50$ K/ps) in the NPT ensemble using the Nosé-Hoover formalism [50] before running an additional 10 ps equilibration at constant T . In this study, simulation timesteps of 1 and 0.2 fs are used respectively for the Potashnikov and SMTB-Q potentials. The simulation cells are finally quenched again to investigate the dislocation core structures after returning at 0 K.

2.3. Dislocation velocity

To compute the dislocation velocity under constant stress and temperature, $v(\tau, T)$, the relaxed configuration of the neutral dipole with a dislocation line length of $24b$ is first heated up to temperatures between 1600 to 2200 K using the NPT ensemble at a heating rate of 50 K/ps. For each temperature,

a constant shear stress $\tau = \tau_{xz}$ is applied using the Nosé-Hoover barostat after a short equilibration time of 10 ps while the other components of the stress tensor are maintained at zero. The dislocation velocity is derived from the Orowan’s equation $\dot{\gamma} = \rho_m b v(\tau, T)$ where $\dot{\gamma}$ is the plastic shear rate here inferred from the simulation cell shape evolution and $\rho_m = 2/(l_x l_z)$ is the mobile dislocation density.

3. Results

3.1. $\frac{1}{2}\langle 110 \rangle \{001\}$ edge dislocation core: neutral vs. charged configurations

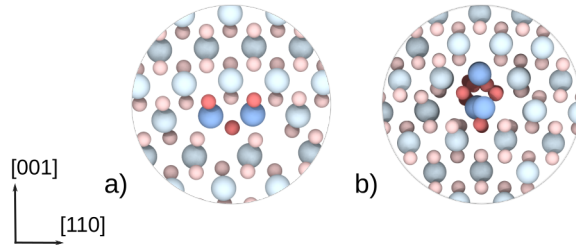


Figure 2: Relaxed configurations of $\frac{1}{2}\langle 110 \rangle \{001\}$ charged dislocation edge cores computed at 0 K using the Potashnikov interatomic potential, (a) positively-charged dislocation core and (b) negatively-charged dislocation core. Atoms colored in red and blue refer respectively to oxygen and uranium.

Figure 2 shows the relaxed configurations of the charged (positive and negative) edge dislocation cores obtained with the Potashnikov potential. The positively charged core presented in Figure 2a is characterized by two columns of $\text{UO}_{1.5}$ molecules *i.e.* two UO columns of atoms that encompass an axis-aligned O column in the centre of the dislocation core region. For the negatively-charged core (Figure 2b), the additional charges force the re-orientation of neighboring UO_2 molecules repelling oxygen atoms. Also, the symmetry of parts of the O columns breaks during energy minimization leading to alternate positions of the O atoms along the dislocation line that better accommodate local charge variations.

The neutral relaxed configuration computed using the Potashnikov potential is shown in Figure 3a. It is characterized by a central UO_2 motif asymmetrically tilted out from the [001] direction towards either the [110] or the $[\bar{1}\bar{1}0]$ direction. There are thus two equivalent variants (left and right) for this core

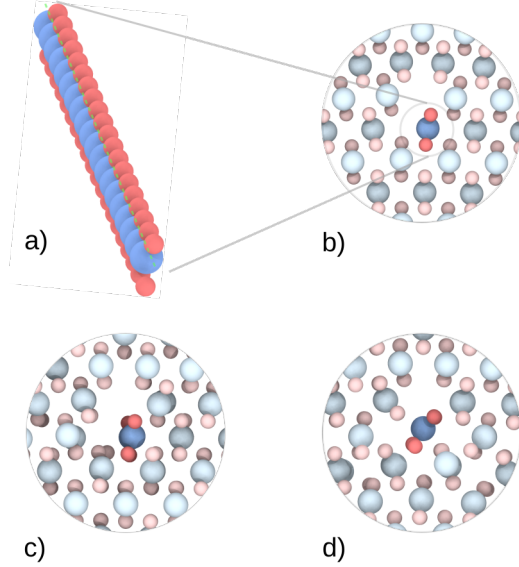


Figure 3: Relaxed configuration of the $\frac{1}{2}\langle 110 \rangle\{001\}$ neutral dislocation edge core computed at 0 K: the Ashbee core, (a) Perspective view along the dislocation line, (b) Potashnikov fixed-charge potential, (c) SMTB-Q variable-charge potential, (d) DFT.

configuration, which corresponds to the asymmetrical Ashbee core detailed in [23]. Relaxed configuration obtained using the SMTB-Q potential and DFT are shown for comparison in Figures 3c and d, respectively. The configuration obtained with DFT is close to that obtained with the Potashnikov potential and differs only by larger rotations of the UO_2 molecules away from the $[001]$ direction. By way of contrast, the SMTB-Q potential still predicts an asymmetrical core but characterized by an alternation of the O atoms along the dislocation line. The Potashnikov potential thus predicts fairly well the Ashbee dislocation core compared to DFT calculations.

The energy difference between E_{dislo}^{Ashbee} and $E_{dislo}^{charged}$ (average over the two charged cores) computed using the Potashnikov potential is $\Delta E = E_{dislo}^{Ashbee} - E_{dislo}^{charged} = -1.66 \text{ eV}/b$. This confirms the higher stability of the neutral Ashbee core when compared to the charged cores.

3.2. High-temperature $\frac{1}{2}\langle 110 \rangle \{001\}$ edge dislocation: the zigzag core

To investigate the $\frac{1}{2}\langle 110 \rangle \{001\}$ edge dislocation core structure in conditions relevant for power transient or accidental conditions, the simulation cell is then heated up using Potashnikov potential. Simulation results show a reconstruction of the dislocation core for $T > 450$ K and maintained at higher temperatures. As illustrated in Figure 4, the new dislocation core configuration breaks the translational symmetry of the Ashbee core. It is formed by an alternation of both left and right variants of the Ashbee core along the dislocation line, thus on average, restoring a symmetrical core. This new *zigzag* dislocation core structure remains stable after an energy minimization from $T = 500$ K *i.e.*, the core does not revert back to the asymmetrical Ashbee configuration. Note that this structure obtained after energy minimization from a high-temperature configuration may contain defects in the periodic succession of both variants along the dislocation line (pseudo-period of $2b$).

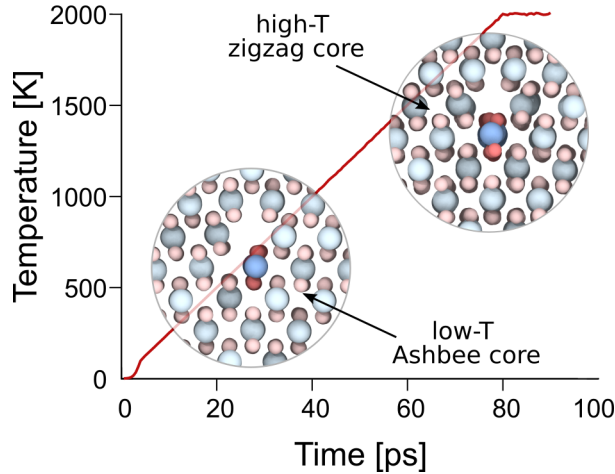


Figure 4: Temperature-induced transformation of the $\frac{1}{2}\langle 110 \rangle \{001\}$ edge dislocation core in UO_2 modeled using Potashnikov potential. The low-temperature Ashbee configuration transformed into a high-temperature *zigzag* configuration for $T > 450$ K.

To further confirm the relevance of the *zigzag* core, the new configuration is further investigated using both potentials and DFT calculations. As an input, we use a handmade *zigzag* core configuration built from the Ashbee core in which O atoms are forced to alternate with a strict period of $2b$ along

the dislocation line. Relaxed *zigzag* core configurations are shown in Figure 5.

Results obtained with the Potashnikov potential confirm the stability of the *zigzag* core here described by the strict alternation of both Ashbee variants with a period of $2b$ (without defects of alternation). While the SMTB-Q *zigzag* core is quantitatively comparable to the one computed with Potashnikov potential, DFT calculations find an even-less symmetrical core where not only the O but also the U atoms in the center of the dislocation core alternate in the $\pm[110]$ directions as seen in Figure 5d.

The *zigzag* core is stable or metastable as no reverse transformation back to the Ashbee core was observed with all three interaction models. One reason for the stability of this core is that it increases the distance between the O atoms in the dislocation core and thus minimizes their Coulombic interaction. Using the Ashbee core energy as a reference, we find $\Delta E = -0.05$ eV/ b using Potashnikov potential, *i.e.* with this energy model, the *zigzag* core is the most stable configuration. With SMTB-Q and DFT calculations, the energy difference is positive, $\Delta E = +0.10$ eV/ b with the former and $\Delta E = +0.25$ eV/ b with the latter, and the *zigzag* core is only metastable. The energy of the *zigzag* core with strict $2b$ period decreases by about 52.5 meV/ b when compared to the configuration obtained from high-temperature quenching (pseudo-period of $2b$).

3.3. $\frac{1}{2}\langle 110 \rangle \{001\}$ edge dislocation mobility

The mobility of the neutral $\frac{1}{2}\langle 110 \rangle \{001\}$ edge dislocation core is investigated using the Potashnikov potential at temperatures ranging from 1600 to 2200 K. In this temperature range, the neutral dislocation core adopts the *zigzag* configuration previously discussed. Constant-temperature MD simulations are performed in the NPT ensemble under shear stresses ranging from 150 to 900 MPa imposed using the Nosé-Hoover barostat. Dislocation velocity results are presented in Figure 6. Two mobility regimes are identified: a non-linear behaviour is observed for low temperatures and stresses, in the blue area highlighted in the figure, while a linear regime is observed at higher stresses and temperatures. Illustrations of typical dislocation glide processes observed in both regimes at 1600 and 2000 K are shown in Figure 7. Kink pairs are clearly visible at low temperature and stress, which is consistent with a Peierls regime of deformation typical of materials with a high lattice friction. By way of contrast, the high stress and temperature regime is characterized by a viscous process without clear evidence of kink-pairs. A

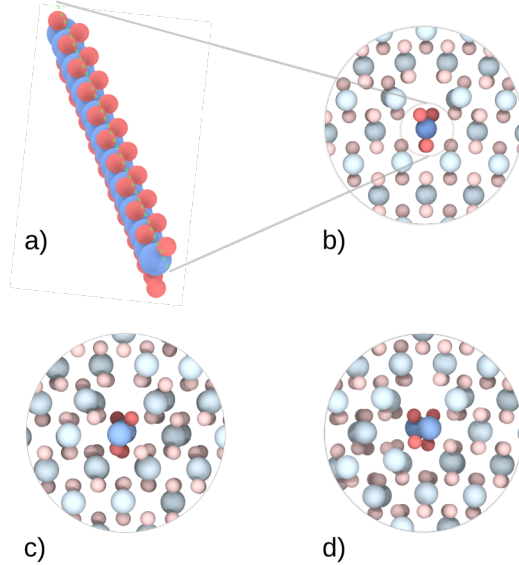


Figure 5: The *zigzag* $\frac{1}{2}\langle 110 \rangle \{001\}$ edge dislocation core in UO_2 computed at 0 K. (a) Illustration of the O atom alternation along the dislocation line, (b) Potashnikov fixed-charge potential, (c) SMTB-Q variable-charge potential, (d) DFT.

transition towards a fully viscous regime is noticed from T of about 2200 K. These velocity curves are discussed below.

4. Discussion

4.1. Dislocation cores

Several $\frac{1}{2}\langle 110 \rangle \{001\}$ edge dislocation core structures are discussed in the literature for UO_2 and other fluorite crystals. First proposed are the theoretical charged cores of Amelinck *et al.* [22] and Evans *et al.* [21] that are sketched in Figure 8a and b. The Amelinckx core is positively charged due to an extra column of O vacancies. It is similar to the core obtained with the Potashnikov potential shown in Figure 2a. Inversely, the Evans core shown in Figure 8b is negatively charged and is significantly different from the one obtained in Figure 2b. Brantley and Bauer [24] have shown that idealized non-stoichiometric edge dislocation cores in UO_2 generate considerable electrostatic fields, which make them more energetic but possibly more mobile when compared to neutral cores. Also, two neutral configurations for the

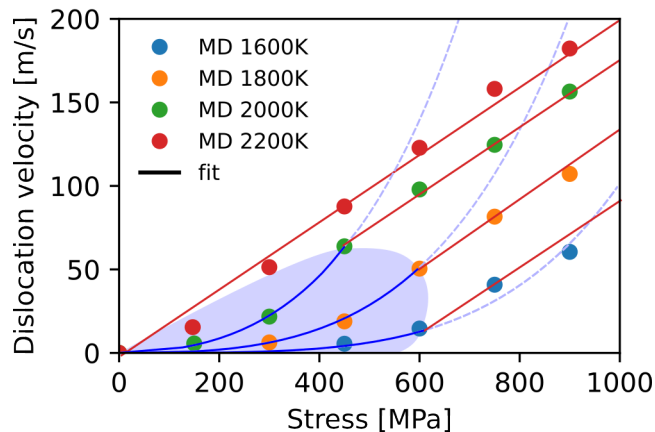


Figure 6: Velocity of the edge $\frac{1}{2}\langle 110 \rangle \{001\}$ edge dislocation in UO_2 as function of an applied shear stress (τ_{xz}) and temperature. Symbols refer to MD data while theoretical adjustments are represented using solid curves. Blue and red solid curves refer to fit processes using the thermally-activated mobility law of Po *et al.* [51] and an athermal viscous mobility law, respectively (Equation 2 and 5). Light-blue domain and dashed curves emphasize the thermally-activated regime and temperature-dependent adjustment extrapolations, respectively.

$\{001\}$ edge dislocation respectively are reported in the literature [23, 24]. As illustrated in Figure 8c and d, the Ashbee and Brantley configurations slightly differ due to the shift of an O column that breaks the symmetry of the Brantley core and results in the asymmetrical Ashbee (left- or right-variant, both being equivalent by symmetry). Here we confirm that the neutral Ashbee core is more stable than charged configurations using the Potashnikov potential.

But our study also shows that the *zigzag* core is a potential candidate for the $\frac{1}{2}\langle 110 \rangle \{001\}$ edge dislocation in UO_2 . When heating using the Potashnikov potential, the Ashbee core transforms into a *zigzag* configuration where parts of the O atoms along the dislocation line alternate positions with a pseudo-period of $2b$. While DFT and SMTB-Q show comparable energy between the Ashbee and *zigzag* cores, both are more prone to stabilize the Ashbee core at 0 K. Nevertheless, additional simulations using the SMTB-Q variable charged potential show that the Ashbee core also evolves into the similar *zigzag* configuration with a pseudo-period of $2b$ when heating in the same temperature range, confirming the reliability of the *zigzag* core at high

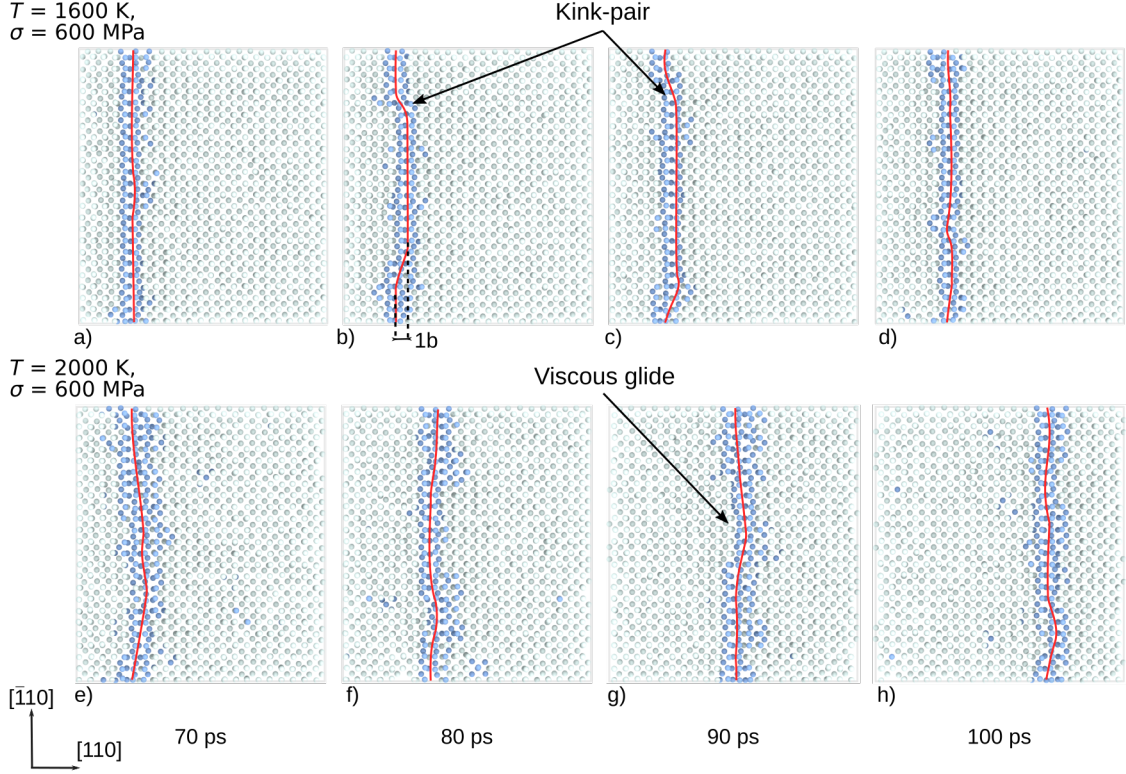


Figure 7: Dislocation glide mechanisms for the $\frac{1}{2}\langle 110 \rangle\{001\}$ edge dislocation ($l = 24b$) computed using the Potashnikov interatomic potential. (a-d) Nucleation and propagation of a kink-pair ($T = 1600 \text{ K}$, $\sigma = 600 \text{ MPa}$) typical of the thermally-activated regime, (e-h) Viscous vibrating string behaviour ($T = 2000 \text{ K}$, $\sigma = 600 \text{ MPa}$). Only the U sublattice is shown for the sake of clarity. Perfect crystal and dislocation atoms are colored in light- and dark-blue, respectively. Red curves are guides for the eyes that emphasize the dislocation shape.

temperature.

It may be generally expected that a defected zigzag core is the stable core at any finite temperature with any energetic model. Indeed, the dislocation core can be viewed as a one-dimensional (1D) system made of UO_2 molecules having two possible tilt directions towards $\pm[110]$. If the interactions between UO_2 molecules are short-ranged (which is expected since the molecules are neutral), the dislocation core is analogous to a 1D Ising model, which is

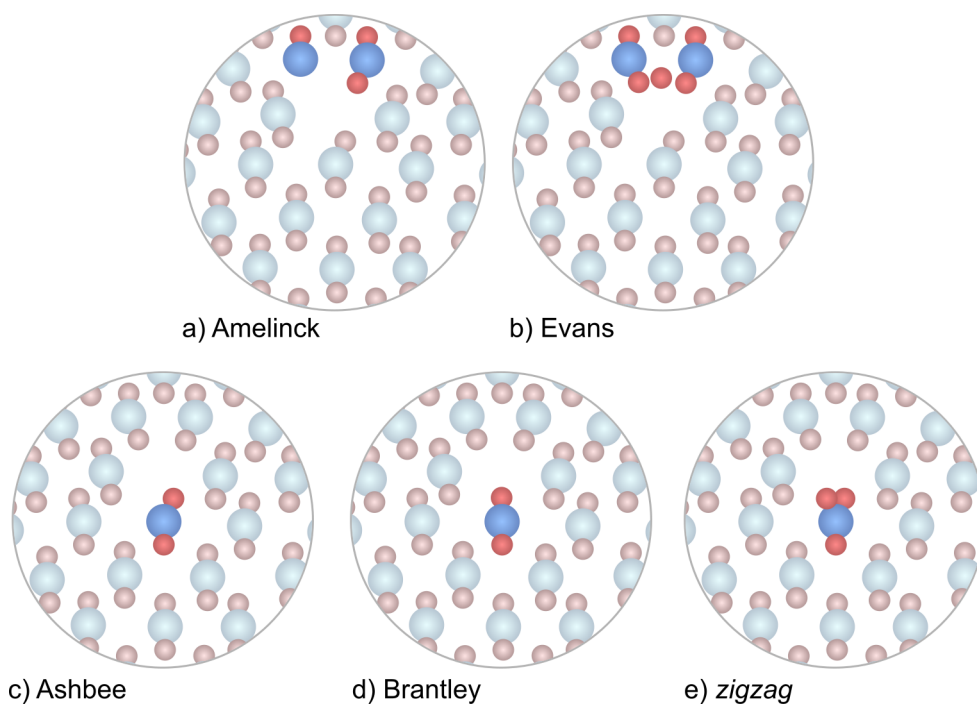


Figure 8: Artworks of the various configurations of the $\frac{1}{2}\langle 110 \rangle \{001\}$ edge dislocation core in UO_2 including the a) Amelincks (positive charge), b) Evans (negative charge), c) asymmetric Ashbee (neutral), d) symmetric Brantley (neutral) and e) the *zigzag* (neutral) core configurations.

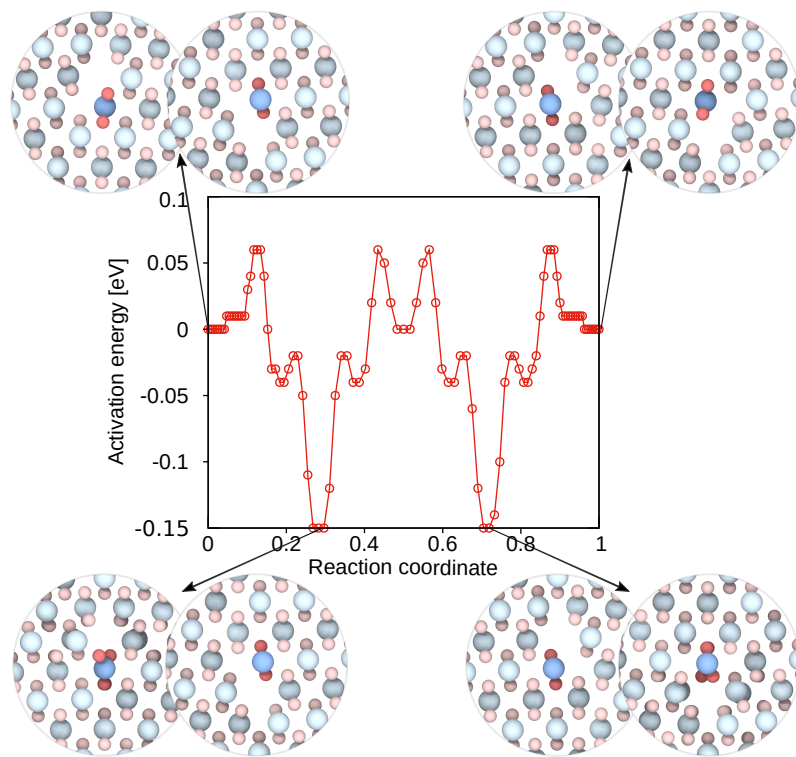


Figure 9: Nudged Elastic Band calculation (Potashnikov potential) of the energy pathway between both variants of the Ashbee core. Inset show the atomic configurations of both dipole dislocations along the path.

known to be disordered at any temperatures [52], *i.e.* it contains a disordered alternation of ± 1 spins, which correspond to the configurations seen here in the MD simulations with a disordered alternation of both Ashbee variants. A disordered state is in fact expected for any 1D system with short-ranged interactions [53]. To check this analogy, we verified that the Ashbee to *zigzag* core transition temperature depends on the heating rate: it decreases from 450 K to 80 K when \dot{T} is decreased from 50 to 10 K/ps.

An additional proof of the *zigzag* core reliability was obtained using the Nudged Elastic Band (NEB) method [54, 55]. Using the left- and right-variants of the Ashbee core as initial and final configurations, we performed a NEB calculation in a dipole cell with a dislocation length of $4b$ to investigate the possible existence of additional configurations with the Potashnikov potential. The calculation is built using 96 replicas of the dislocation dipole with initial and final configurations made of relaxed asymmetric Ashbee cores. A spring constant of $1 \text{ eV}/\text{\AA}^{-1}$ was used with a force tolerance for convergence of $0.01 \text{ eV}/\text{\AA}$. Figure 9 shows the relaxed transition path as well as selected atomic configurations in the insets. For each inset, two dislocation cores corresponding to both dislocation cores of the dislocation dipole are illustrated. As presumed, the final configuration shows the exact same energy as the initial configuration, which confirms that right- and left-side Ashbee cores are strictly identical. Along the NEB path, both dipole cores do not transition simultaneously. One core transits between images 0 to 48 and the other core, between images 48 and 96. During both transitions, the transforming core passes through a *zigzag* core as illustrated by both atomic configuration at the bottom of Figure 9. This results in two local energy minima at images 24 and 72. The energy of -0.15 eV is slightly larger than the -0.20 eV (for a $4b$ length) expected from the energy difference between Ashbee and the *zigzag* cores found in Section 3.2. This is due to the NEB constraint which does not allow the image to fully reach the energy minimum. Interestingly, the initial energy path was obtained from a linear interpolation between the initial and final configurations and thus contained a saddle configuration close to a symmetrical Brantley core. But this core spontaneously transforms into a *zigzag* core during the energy minimization, which confirms the instability of the Brantley core and the stability of the *zigzag* core, at least with the Potashnikov potential.

4.2. Dislocation mobility

The mobility of the *zigzag* core is investigated using the Potashnikov potential in Figure 6. The velocities computed here are about 25 to 50% slower than those reported by Lunev *et al.* with the same potential, slip system and dislocation character [15]. We attribute this difference to the dislocation core that is probably charged in Lunev’s study since the authors used a simulation cell containing a single dislocation. If true, this might confirm Brantley’s hypothesis about primary dislocations in UO_2 : charged dislocations are energetically less favorable but glide more easily. Nevertheless, no experimental data are currently available to conclude on the dislocation core stoichiometry in UO_2 .

Soulié *et al.* have shown that the kink-pair migration energy is particularly significant for the $\frac{1}{2}\langle 110 \rangle \{001\}$ edge dislocation in UO_2 . In this context and without explicit data for kink-pair nucleation/migration energies, we adjusted our MD data using a two-steps process. First, we use the mobility law of Po *et al.* [51] derived from the kink model of Hirth and Lothe [46] to account for both kink-pair nucleation and propagation energies to model the thermally-activated mobility of the dislocation $v_{kp}(\tau, T)$:

$$v_{kp}(\tau, T) = \frac{\tau b}{B(\tau, T)} \exp\left(-\frac{\Delta G_{kp}(\tau, T)}{2k_B T}\right), \quad (2)$$

with $k_B T$ is the Boltzmann factor, $\Delta G_{kp}(\tau, T)$ the free energy of kink-pair nucleation and migration expressed using the Kocks formalism [56] and a linear entropy approximation:

$$\Delta G_{kp}(\tau, T) = \Delta H_0 \left(\left(1 - \left(\frac{\tau}{\tau_P}\right)^p\right)^q - T/T_0 \right), \quad (3)$$

where ΔH_0 is the kink-pair enthalpy at zero stress, p and q are Kocks parameters and T_0 is a transition temperature that scales with the melting temperature T_m . $B(\tau, T)$ is a drag coefficient that depends on stress and temperature,

$$B(\tau, T) = \frac{a \left(2a \exp\left(-\frac{\Delta G_{kp}(\tau, T)}{2k_B T}\right) + l \right)}{2hL} B_k, \quad (4)$$

where a is the periodicity of the secondary Peierls barrier, $l=24b$ is the dislocation length, h the kink-pair height and B_k a drag constant.

We used a least-square method to adjust a set of parameters including ΔH_0 , τ_P , B_k , p and q for three of the temperature data-sets. MD data selected for the fit and model predictions are shown in blue in Figure 6.

Secondly, the overdamped regime (Figure 6, red curves) at high temperature and stress is adjusted using a viscous law and a damping coefficient B independent of the temperature,

$$v(\tau) = v_0 + \frac{\tau b}{B}. \quad (5)$$

Here, the viscous law (Equation 5) is characterized by a constant term v_0 to adjust the zero stress limit. Note that this term has only a fitting purpose as the thermally-activated mobility of the dislocation is described in the low-stress regime by Equation 2.

Dislocation velocities computed here in the classical MD range of strain-rates ($\dot{\epsilon} \sim 10^8$ - 10^9 /s) show a transition from the thermally-activated regime towards the fully overdamped regime for T_a about 2200 K. As discussed *e.g.*, in Ref. 57, T_a can decrease of several hundred Kelvin when reducing the strain rate by several orders of magnitude *i.e.*, here down to the experimental strain-rate. Thus, we can assume that T_a is here in qualitative good agreement with experimental $T_a^{exp} \sim 1750$ K in the $\frac{1}{2}\langle 110 \rangle \{001\}$ slip systems 6, 9, 58. For $T < T_a$, the transition is still observable but only for stresses larger than a critical stress τ_v , which decreases when increasing the temperature (down to $\tau_v=0$ for $T \geq T_a$).

Fitting parameters for both mobility laws are provided in Table 1. The adjusted Peierls stress $\tau_P=4.4$ GPa is in good agreement with the results of Soulié *et al.* ($\tau_P=3.9$ GPa) obtained using the SMTB-Q potential. On the other hand, the kink-pair energy ($\Delta H_0=3.67$ eV) is also comparable to Soulié *et al.* results who obtained up to 2.93 eV for non-stoichiometric kinks using the NEB method.

In the literature, the viscous drag coefficient is generally assumed to be controlled by a temperature-dependent phonon drag process leading to $B(T)=\sum_n B_n T^n$ 59, 60. Here, B does not depend on the temperature and we calculate $B=B_0=2.2 \cdot 10^{-3}$ Pa.s when averaging on the four temperature data-sets. This result contradicts classical observations made for FCC 61, 62 (or BCC edge dislocations 63, 51) where B is in the $\sim 10^{-5}$ Pa.s range but varies with temperature in agreement with the phonon scattering theory. However, temperature-independent B was reported for screw dislocations in BCC metals 64, 51 and alkali-halides 65, 66 in the same $\sim 10^{-3}$ Pa.s range, these sys-

Parameters	
a_0 (Å)	5.47
b (Å)	$a_0/\sqrt{2}$
L (Å)	$24b$
h (Å)	b
a (Å)	b
T_m (K)	3300
T_0 (K)	$2640 (0.8 \times T_m)$
Data	
τ_P (GPa)	4.42
ΔH_0 (eV)	3.67
p	0.71
q	1.0
B_k ($\times 10^{-3}$ Pa.s)	3.03
B_0 ($\times 10^{-3}$ Pa.s)	2.22

Table 1: Dislocation mobility parameters for the neutral $\frac{1}{2}\langle 110 \rangle \{001\}$ edge dislocation in UO_2 . Data are adjusted on MD data computed on the 1600 to 2200 K temperature range.

tems being characterized by a high-lattice friction as UO_2 . Arguments about the velocity weakening due to near transonic dislocation velocity regime exist in FCC metals and alkali-halides [65, 62], but this does not fit our results since the present velocities are well below the longitudinal sound velocity of UO_2 (~ 5165 m/s [67]). Only few information can be found about a possible transition from a thermally-activated, *BCC-like*, regime to a dynamic, *FCC-like*, regime in lattice-friction materials. Al’shitz suggests that when the kinetic energy of the dislocation overshoots the Peierls energy, the dominant dislocation dissipation process relies on the transfer of the dislocation energy into lattice vibrations (phonons), especially at high-temperature [68, 69, 63]. Several phonon mechanisms can be involved but only phonon radiation (due to the Peierls relief) or slow phonons can generate a temperature-independent drag coefficient in contrast with the classical phonon scattering. Swinburne and collaborators explain that the temperature-independent drag term arises because the vibrations orthogonal to the defect motion direction are different than perfect crystal eigenmodes, an assumption not included in phonon scattering theoretical approaches that justify B variations with temperature [70, 51]. While the authors confirm that the temperature-independent term

might dominate for nanoscale defects in BCC metals (as lattice friction tends to diminish the temperature dependence of B) no strict application nor model applied to dislocations can be found in the current literature. This finding reopens the debate on the athermal mobility of dislocations in high lattice-friction materials.

5. Conclusion

In this work, we investigated both the static and dynamical properties of the $\frac{1}{2}\langle 110 \rangle \{001\}$ edge dislocation, which plays a significant role in the plastic behavior of UO_2 ceramics. In contrast with many materials where edge dislocations have a simpler core structure and dynamics than screw dislocations, the edge dislocation in UO_2 can adopt many different core structures, charged or neutral. We have confirmed that charged cores have a much higher energy than neutral cores, and are thus less expected to play a role in UO_2 plasticity. Among the neutral cores, the asymmetrical Ashbee core is expected to have the lowest energy. However, we found that a so-far unreported zigzag core has an energy comparable, if not lower, than the Ashbee core. Moreover, while previous studies focused on 0 K calculations, we have shown that a defected zigzag core, made of a disordered succession of both variants of the Ashbee core, is stabilized at all finite temperatures due to entropy effect. While the 0 K stability of the dislocation cores strongly depends on the energetic model, the finite-temperature stabilization results from a general argument applied to one-dimensional systems. We thus expect that a defected zigzag core should prevail in experimental UO_2 ceramics.

We also studied the mobility of the defected zigzag core. Its velocity can be accurately represented by a mobility law based on a thermally-activated kink-pair mechanism at low temperature and stress and a linear regime at high temperature or stress. Interestingly, we found that the drag coefficient in the linear regime does not depend on the temperature, as observed in other high-Peierls materials, but in contrast with FCC metals. The mobility law determined here can be used in higher-scale models and in particular in dislocation dynamics simulations to study plasticity at the micron-scale in UO_2 . This work is currently underway.

6. Acknowledgements

This research is achieved in the framework of a simulation project devoted to the PLEIADES fuel software environment funding by the French nuclear institute between CEA, EDF and FRAMATOME.

References

- [1] M. Oguma, Cracking and relocation behavior of nuclear fuel pellets during rise to power, *Nuclear engineering and design* 76 (1) (1983) 35–45. [doi:10.1016/0029-5493\(83\)90045-6](https://doi.org/10.1016/0029-5493(83)90045-6).
- [2] B. Michel, J. Sercombe, G. Thouvenin, R. Chatelet, 3D fuel cracking modelling in pellet cladding mechanical interaction, *Engineering fracture mechanics* 75 (11) (2008) 3581–3598. [doi:10.1016/j.engfracmech.2006.12.014](https://doi.org/10.1016/j.engfracmech.2006.12.014).
- [3] C. S. Yust, C. J. McHargue, Dislocation substructures in deformed uranium dioxide single crystals, *Journal of Nuclear Materials* 31 (2) (1969) 121 – 137. [doi:10.1016/0022-3115\(69\)90187-1](https://doi.org/10.1016/0022-3115(69)90187-1).
- [4] M. S. Seltzer, A. H. Clauer, B. A. Wilcox, The influence of stoichiometry on compression creep of uranium dioxide single crystals, *Journal of Nuclear Materials* 44 (1) (1972) 43 – 56. [doi:10.1016/0022-3115\(72\)90127-4](https://doi.org/10.1016/0022-3115(72)90127-4).
- [5] A. Alamo, J. M. Lefèbvre, J. Soullard, Deformation plastique du bioxyde d’uranium: Observation des sous-structures de dislocations, *Journal of Nuclear Materials* 75 (1) (1978) 145 – 153. [doi:10.1016/0022-3115\(78\)90038-7](https://doi.org/10.1016/0022-3115(78)90038-7).
- [6] J. Byron, The yield and flow of single crystals of uranium dioxide, *Journal of Nuclear Materials* 28 (1) (1968) 110–114. [doi:10.1016/0022-3115\(68\)90062-7](https://doi.org/10.1016/0022-3115(68)90062-7).
- [7] J. S. Nadeau, Dependence of flow stress on nonstoichiometry in oxygen-rich uranium dioxide at high temperatures, *Journal of the American Ceramic Society* 52 (1) (1969) 1 – 7. [doi:10.1111/j.1151-2916.1968.tb11863.x-i1](https://doi.org/10.1111/j.1151-2916.1968.tb11863.x-i1).

- [8] P. T. Sawbridge, E. C. Sykes, Dislocation glide in UO_2 single crystals at 1600°K, *Philosophical Magazine A* 24 (187) (1971) 33 – 53. [doi:10.1080/14786437108216422](https://doi.org/10.1080/14786437108216422).
- [9] J.-M. Lefebvre, Contribution à l'étude de la déformation plastique d'une céramique de structure fluorite : le bioxyde d'uranium, Ph.D. thesis, faculté des sciences de Poitiers (1977).
- [10] R. J. Keller, T. E. Mitchell, A. H. Heuer, Plastic deformation in non-stoichiometric UO_{2+x} single crystals—II. Deformation at high temperatures, *Acta Metallurgica* 36 (4) (1988) 1073 – 1083. [doi:10.1016/0001-6160\(88\)90161-7](https://doi.org/10.1016/0001-6160(88)90161-7).
- [11] D. C. Parfitt, C. L. Bishop, M. R. Wenman, R. W. Grimes, Strain fields and line energies of dislocations in uranium dioxide., *Journal of physics. Condensed matter : an Institute of Physics journal* 22 (17) (2010) 175004. [doi:10.1088/0953-8984/22/17/175004](https://doi.org/10.1088/0953-8984/22/17/175004).
- [12] P. Fossati, L. V. Brutzel, B. Devincere, Molecular dynamics simulation of dislocations in uranium dioxide, *Journal of Nuclear Materials* 443 (1-3) (2013) 359 – 365. [doi:10.1016/j.jnucmat.2013.07.059](https://doi.org/10.1016/j.jnucmat.2013.07.059).
- [13] R. Skelton, A. M. Walker, Peierls-Nabarro modeling of dislocations in UO_2 , *Journal of Nuclear Materials* 495 (2017) 202 – 210. [doi:10.1016/j.jnucmat.2017.08.024](https://doi.org/10.1016/j.jnucmat.2017.08.024).
- [14] A. Soulié, J.-P. Crocombette, A. Kraych, F. Garrido, G. Sattonnay, E. Clouet, Atomistically-informed thermal glide model for edge dislocations in uranium dioxide, *Acta Materialia* 150 (2018) 248 – 261. [doi:10.1016/j.actamat.2018.03.024](https://doi.org/10.1016/j.actamat.2018.03.024).
- [15] A. V. Lunev, A. Y. Kuksin, S. V. Starikov, Glide mobility of the $1/2[110](001)$ edge dislocation in UO_2 from molecular dynamics simulation, *International Journal of Plasticity* 89 (2017) 85 – 95. [doi:10.1016/j.ijplas.2016.11.004](https://doi.org/10.1016/j.ijplas.2016.11.004).
- [16] E. Yakub, C. Ronchi, D. Staicu, Molecular dynamics simulation of pre-melting and melting phase transitions in stoichiometric uranium dioxide, *The Journal of Chemical Physics* 127 (9) (2007) 094508. [doi:10.1063/1.2764484](https://doi.org/10.1063/1.2764484).

- [17] N. D. Morelon, D. Ghaleb, J. M. Delaye, L. V. Brutzel, A new empirical potential for simulating the formation of defects and their mobility in uranium dioxide, *Philosophical Magazine A* 83 (13) (2003) 1533 – 1555. [doi:10.1080/1478643031000091454](https://doi.org/10.1080/1478643031000091454).
- [18] S. I. Potashnikov, A. S. Boyarchenkov, K. A. Nekrasov, A. Y. Kupryazhkin, High-precision molecular dynamics simulation of $\text{UO}_2\text{-PuO}_2$: Pair potentials comparison in UO_2 , *Journal of Nuclear Materials* 419 (1-3) (2011) 217 – 225. [doi:10.1016/j.jnucmat.2011.08.033](https://doi.org/10.1016/j.jnucmat.2011.08.033).
- [19] M. W. D. Cooper, M. J. D. Rushton, R. W. Grimes, A many-body potential approach to modelling the thermomechanical properties of actinide oxides, *Journal of Physics: Condensed Matter* 26 (10) (2014) 105401. [doi:10.1088/0953-8984/26/10/105401](https://doi.org/10.1088/0953-8984/26/10/105401).
- [20] L. Pauling, The nature of the chemical bond. IV. The energy of single bonds and the relative electronegativity of atoms, *Journal of the American Chemical Society* 54 (9) (1932) 3570–3582. [doi:10.1021/ja01348a011](https://doi.org/10.1021/ja01348a011).
- [21] A. G. Evans, P. L. Pratt, Dislocations in the fluorite structure, *Philosophical Magazine* 20 (168) (1969) 1213–1237. [doi:10.1080/14786436908228207](https://doi.org/10.1080/14786436908228207).
- [22] S. Amelinckx, Dislocations in ionic crystals, *Il Nuovo Cimento* 7 (S2) (1958) 569–599. [doi:10.1007/BF02751495](https://doi.org/10.1007/BF02751495).
- [23] K. H. G. Ashbee, F. C. Frank, Dislocations in the fluorite structure, *Philosophical Magazine* 21 (169) (1970) 211–213. [doi:10.1080/14786437008238410](https://doi.org/10.1080/14786437008238410).
- [24] W. A. Brantley, C. L. Bauer, Geometric Analysis of Charged Dislocations in the Fluorite Structure, *Physica Status Solidi (b)* 40 (2) (1970) 707–715. [doi:10.1002/pssb.19700400231](https://doi.org/10.1002/pssb.19700400231).
- [25] S. Plimpton, Fast parallel algorithms for short-range molecular-dynamics, *Journal of Computational Physics* 117 (1) (1995) 1 – 19. [doi:10.1006/jcph.1995.1039](https://doi.org/10.1006/jcph.1995.1039).

- [26] E. Maras, N. Salles, R. Tétot, T. Ala-Nissila, H. Jónsson, Improved tight-binding charge transfer model and calculations of energetics of a step on the rutile TiO_2 (110) surface, *The Journal of Physical Chemistry C* 119 (19) (2015) 10391–10399. [doi:10.1021/acs.jpcc.5b01580](https://doi.org/10.1021/acs.jpcc.5b01580).
- [27] N. Salles, O. Politano, E. Amzallag, R. Tétot, Molecular dynamics study of high-pressure alumina polymorphs with a tight-binding variable-charge model, *Computational Materials Science* 111 (C) (2016) 181 – 189. [doi:10.1016/j.commatsci.2015.09.017](https://doi.org/10.1016/j.commatsci.2015.09.017).
- [28] A. V. Lunev, S. V. Starikov, T. N. Aliev, V. I. Tseplyaev, Understanding thermally-activated glide of $1/2\langle 110 \rangle\{110\}$ screw dislocations in UO_2 – A molecular dynamics analysis, *International Journal of Plasticity* 110 (2018) 294 – 305. [doi:10.1016/j.ijplas.2018.07.003](https://doi.org/10.1016/j.ijplas.2018.07.003).
- [29] P. P. Ewald, Die berechnung optischer und elektrostatischer gitterpotentiale, *Annalen der Physik* 369 (3) (1921) 253–287.
- [30] D. Wolf, P. Keblinski, S. Phillpot, J. Eggebrecht, Exact method for the simulation of coulombic systems by spherically truncated, pairwise r^{-1} summation, *The Journal of Chemical Physics* 110 (17) (1999) 8254–8282. [doi:10.1063/1.478738](https://doi.org/10.1063/1.478738).
- [31] P. E. Blöchl, O. Jepsen, O. K. Andersen, Improved tetrahedron method for brillouin-zone integrations, *Physical Review B* 49 (23) (1994) 16223. [doi:PhysRevB.49.16223](https://doi.org/10.1103/PhysRevB.49.16223).
- [32] G. Kresse, D. Joubert, From ultrasoft pseudopotentials to the projector augmented-wave method, *Physical Review B* 59 (3) (1999) 1758. [doi:10.1103/PhysRevB.59.1758](https://doi.org/10.1103/PhysRevB.59.1758).
- [33] J. P. Perdew, K. Burke, M. Ernzerhof, Generalized gradient approximation made simple, *Physical Review Letters* 77 (18) (1996) 3865. [doi:10.1103/PhysRevLett.77.3865](https://doi.org/10.1103/PhysRevLett.77.3865).
- [34] A. Lichtenstein, M. Katsnelson, Ab initio calculations of quasiparticle band structure in correlated systems: LDA++ approach, *Physical Review B* 57 (12) (1998) 6884. [doi:10.1103/PhysRevB.57.6884](https://doi.org/10.1103/PhysRevB.57.6884).

- [35] J. Wiktor, M.-F. Barthe, G. Jomard, M. Torrent, M. Freyss, M. Bertolus, Coupled experimental and DFT+U investigation of positron lifetimes in UO_2 , *Physical Review B* 90 (2014) 184101. [doi:10.1103/PhysRevB.90.184101](https://doi.org/10.1103/PhysRevB.90.184101).
- [36] R. Bès, P. Martin, E. Vathonne, R. Delorme, C. Sabathier, M. Freyss, M. Bertolus, P. Glatzel, Experimental evidence of Xe incorporation in Schottky defects in UO_2 , *Applied Physics Letters* 106 (2015) 114102. [doi:10.1063/1.4914300](https://doi.org/10.1063/1.4914300).
- [37] E. Vathonne, D. A. Andersson, M. Freyss, R. Perriot, M. W. D. Cooper, C. R. Stanek, M. Bertolus, Determination of krypton diffusion coefficients in uranium dioxide using atomic scale calculations, *Inorganic Chemistry* 56 (2017) 125. [doi:10.1021/acs.inorgchem.6b01560](https://doi.org/10.1021/acs.inorgchem.6b01560).
- [38] F. Bruneval, M. Freyss, J.-P. Crocombette, Lattice constant in nonstoichiometric uranium dioxide from first principles, *Physical Review Materials* 2 (2018) 023801. [doi:10.1103/PhysRevMaterials.2.023801](https://doi.org/10.1103/PhysRevMaterials.2.023801).
- [39] B. Dorado, B. Amadon, M. Freyss, M. Bertolus, DFT+U calculations of the ground state and metastable states of uranium dioxide, *Physical Review B* 79 (23) (2009) 235125. [doi:10.1103/PhysRevB.79.235125](https://doi.org/10.1103/PhysRevB.79.235125).
- [40] G. Amoretti, A. Blaise, R. Caciuffo, J. M. Fournier, M. T. Hutchings, R. Osborn, A. D. Taylor, 5f-electron states in uranium dioxide investigated using high-resolution neutron spectroscopy, *Physical Review B* 40 (1989) 1856. [doi:10.1103/PhysRevB.40.1856](https://doi.org/10.1103/PhysRevB.40.1856).
- [41] A. Stukowski, Visualization and analysis of atomistic simulation data with OVITO—the Open Visualization Tool, *Modelling and Simulation in Materials Science and Engineering* 18 (1) (2010-01) 7pp. [doi:10.1088/0965-0393/18/1/015012](https://doi.org/10.1088/0965-0393/18/1/015012).
- [42] P. M. Larsen, S. Schmidt, J. Schiøtz, Robust structural identification via polyhedral template matching, *Modelling and Simulation in Materials Science and Engineering* 24 (5) (2016) 055007 – 19. [doi:10.1088/0965-0393/24/5/055007](https://doi.org/10.1088/0965-0393/24/5/055007).
- [43] W. Cai, V. V. Bulatov, J. Chang, J. Li, S. Yip, Periodic image effects in dislocation modelling, *Philosophical Magazine A* 83 (5) (2003) 539–567. [doi:10.1080/0141861021000051109](https://doi.org/10.1080/0141861021000051109).

- [44] D. Rodney, L. Ventelon, E. Clouet, L. Pizzagalli, F. Willaime, Ab initio modeling of dislocation core properties in metals and semiconductors, *Acta Materialia* 124 (2017) 633 – 659. [doi:10.1016/j.actamat.2016.09.049](https://doi.org/10.1016/j.actamat.2016.09.049).
- [45] P. Hirel, AtomsK: A tool for manipulating and converting atomic data files, *Computer Physics Communications* 197 (2015) 212 – 219. [doi:10.1016/j.cpc.2015.07.012](https://doi.org/10.1016/j.cpc.2015.07.012).
- [46] J. P. Hirth, J. Lothe, *Theory of dislocations*, John Wiley and Sons, 1982.
- [47] D. J. Bacon, Y. N. Osetsky, D. Rodney, Chapter 88 Dislocation–Obstacle Interactions at the Atomic Level, Vol. 15 of *Dislocations in Solids*, Elsevier, 2009, pp. 1 – 90. [doi:10.1016/S1572-4859\(09\)01501-0](https://doi.org/10.1016/S1572-4859(09)01501-0).
- [48] E. Bitzek, P. Koskinen, F. Gähler, M. Moseler, Structural relaxation made simple, *Physical Review Letters* 97 (2006) 170201. [doi:10.1103/physrevlett.97.170201](https://doi.org/10.1103/physrevlett.97.170201).
- [49] E. Clouet, L. Ventelon, F. Willaime, Dislocation Core Energies and Core Fields from First Principles, *Physical Review Letters* 102 (5) (2009) 055502. [doi:10.1103/physrevlett.102.055502](https://doi.org/10.1103/physrevlett.102.055502).
- [50] S. Nosé, A molecular dynamics method for simulations in the canonical ensemble, *Molecular Physics* 52 (2) (1984) 255 – 268. [doi:10.1080/00268978400101201](https://doi.org/10.1080/00268978400101201).
- [51] G. Po, Y. Cui, D. Rivera, D. Cereceda, T. D. Swinburne, J. Marian, N. Ghoniem, A phenomenological dislocation mobility law for bcc metals, *Acta Materialia* 119 (C) (2016) 123–135. [doi:10.1016/j.actamat.2016.08.016](https://doi.org/10.1016/j.actamat.2016.08.016).
- [52] L. P. Kadanoff, *Statistical physics: statics, dynamics and renormalization*, World Scientific, 2000.
- [53] N. D. Mermin, Crystalline Order in Two Dimensions, *Physical Review* 176 (1) (1968) 250–254. [doi:10.1103/physrev.176.250](https://doi.org/10.1103/physrev.176.250).

- [54] H. Jonsson, G. Mills, K. W. Jacobsen, Nudged elastic band method for finding minimum energy paths of transitions, world scientific Edition, Classical and quantum dynamics in condensed phase simulations, World Scientific, Singapore, 1998, pp. 385 – 404. [doi:10.1142/9789812839664_0016](https://doi.org/10.1142/9789812839664_0016).
- [55] G. Henkelman, B. P. Uberuaga, H. Jónsson, A climbing image nudged elastic band method for finding saddle points and minimum energy paths, The Journal of Chemical Physics 113 (22) (2000) 9901 – 9904. [doi:10.1063/1.1329672](https://doi.org/10.1063/1.1329672).
- [56] U. F. Kocks, A. S. Argon, M. F. Ashby, Thermodynamics and Kinetics of Slip, Pergamon, Pergamon, 1975.
- [57] P. Cordier, J. Amodeo, P. Carrez, Modelling the rheology of MgO under Earth’s mantle pressure, temperature and strain rates, Nature 481 (7380) (2012) 177 – 180. [doi:10.1038/nature10687](https://doi.org/10.1038/nature10687).
- [58] L. Portelette, J. Amodeo, R. Madec, J. Soulacroix, T. Helfer, B. Michel, Crystal viscoplastic modeling of UO₂ single crystal, Journal of Nuclear Materials 510 (2018) 635–643. [doi:10.1016/j.jnucmat.2018.06.035](https://doi.org/10.1016/j.jnucmat.2018.06.035).
- [59] G. Leibfried, Über den Einfluß thermisch angeregter Schallwellen auf die plastische Deformation, Zeitschrift für Physik 127 (4) (1950) 344–356. [doi:10.1007/bf01329831](https://doi.org/10.1007/bf01329831).
- [60] E. Nadgorny, Dislocation dynamics and mechanical properties of crystals, Progress in Materials Science 31 (1988) 1–530. [doi:10.1016/0079-6425\(88\)90005-9](https://doi.org/10.1016/0079-6425(88)90005-9).
- [61] E. Bitzek, P. Gumbsch, Dynamic aspects of dislocation motion: atomistic simulations, Materials Science and Engineering A 400 (2005) 40 – 44. [doi:10.1016/j.msea.2005.03.047](https://doi.org/10.1016/j.msea.2005.03.047).
- [62] D. L. Olmsted, L. G. H. Jr, W. A. Curtin, R. J. Clifton, Atomistic simulations of dislocation mobility in Al, Ni and Al/Mg alloys, Modelling and Simulation in Materials Science and Engineering 13 (3) (2005) 371. [doi:10.1088/0965-0393/13/3/007](https://doi.org/10.1088/0965-0393/13/3/007).

- [63] A. Y. Kuksin, A. V. Yanilkin, Atomistic simulation of the motion of dislocations in metals under phonon drag conditions, *Physics of the Solid State* 55 (5) (2013) 1010–1019. [doi:10.1134/s1063783413050193](https://doi.org/10.1134/s1063783413050193).
- [64] M. R. Gilbert, S. Queyreau, J. Marian, Stress and temperature dependence of screw dislocation mobility in α -Fe by molecular dynamics, *Physical Review B* 84 (17) (2011) 174103. [doi:10.1103/physrevb.84.174103](https://doi.org/10.1103/physrevb.84.174103).
- [65] W. G. Johnston, J. J. Gilman, Dislocation Velocities, Dislocation Densities, and Plastic Flow in Lithium Fluoride Crystals, *Journal of Applied Physics* 30 (2) (1959) 1 – 16. [doi:0.1063/1.1735121](https://doi.org/0.1063/1.1735121).
- [66] J. W. Martin, R. Paetsch, Generalised Viscosity and Dislocation Damping Constant in Diatomic Crystalline Solids, *Physica Status Solidi (b)* 74 (2) (1976) 761–772. [doi:10.1002/pssb.2220740238](https://doi.org/10.1002/pssb.2220740238).
- [67] A. Padel, C. D. Novion, Constantes elastiques des carbures, nitrures et oxydes d’uranium et de plutonium, *Journal of Nuclear Materials* 33 (1) (1969) 40–51. [doi:10.1016/0022-3115\(69\)90006-3](https://doi.org/10.1016/0022-3115(69)90006-3).
- [68] V. A. Al’shitz, V. L. Indenbom, Dynamic dragging of dislocations, *Soviet Physics Uspekhi* 18 (1) (1975) 1–20. [doi:10.1070/pu1975v018n01abeh004689](https://doi.org/10.1070/pu1975v018n01abeh004689).
- [69] V. Alshits, CHAPTER 11 The Phonon-Dislocation Interaction and its Rôle in Dislocation Dragging and Thermal Resistivity, *Modern Problems in Condensed Matter Sciences* 31 (1992) 625–697. [doi:10.1016/b978-0-444-88773-3.50018-2](https://doi.org/10.1016/b978-0-444-88773-3.50018-2).
- [70] T. D. Swinburne, S. L. Dudarev, Phonon drag force acting on a mobile crystal defect: Full treatment of discreteness and nonlinearity, *Physical Review B* 92 (13) (2015) 134302. [arXiv:1506.08731](https://arxiv.org/abs/1506.08731), [doi:10.1103/physrevb.92.134302](https://doi.org/10.1103/physrevb.92.134302).